# Enhancement of Electrocatalytic Activity for Both Hydrogen and Oxygen Evolution Reactions in a Perovskite Oxide

Surendra B. Karki[a], Antonis N. Andriotis[b], Madhu Menon[c], Farshid Ramezanipour[a,*]

[a]Department of Chemistry, University of Louisville, Louisville, Kentucky 40292, USA
[b]Institute of Electronic Structure and Laser, FORTH, Heraklio, Crete, Greece
[c]Conn Center for Renewable Energy Research, University of Louisville, Louisville, KY 40292, USA
*Corresponding author. Email: farshid.ramezanipour@louisville.edu, Phone: +1(502) 852-7061

**Abstract.** We have used both experimental and computational methods to show the significant impact of the incorporation of a 4d metal, Mo, into the perovskite oxide $Ba_{0.5}Sr_{0.5}Co_{0.8}Fe_{0.2}O_{3-\delta}$ (BSCF), which is known as a benchmark electrocatalyst for the anodic reaction of water-splitting. We demonstrate the enhanced electrocatalytic properties of the resulting catalytic material, $Ba_{0.5}Sr_{0.5}Co_{0.5}Mo_{0.5}O_3$ ($BaSrCoMoO_6$), where the presence of the 4d metal Mo leads to the formation of a double perovskite structure, as opposed to the simple perovskite structure of BSCF. The consequence of this transformation is the enhancement of the electrocatalytic properties of $BaSrCoMoO_6$ over BSCF for both half reactions of water-splitting, i.e., hydrogen evolution reaction (HER) and oxygen evolution reaction (OER). Furthermore, $BaSrCoMoO_6$ shows electrocatalytic activity for HER and OER in bulk form without additives, even carbon black, which is commonly added to HER and OER catalysts, including BSCF. Experiments for $BaSrCoMoO_6$ with or without carbon black lead to similar overpotentials. Density functional theory (DFT) calculations reveal the effect of the structural transformation on the shift of the transition metal *d* bands toward the Fermi level, which correlates with the enhanced electrocatalytic activity.

Keywords: Water splitting, Perovskite oxide, Bifunctional electrocatalyst

## 1. Introduction

Among advanced renewable energy technologies, the electrocatalytic water splitting is of considerable interest.[1] It provides an excellent route for utilization of renewable energy and generation of hydrogen. However, the sluggish kinetics of this process needs to be improved by catalyzing its two half-reactions, namely hydrogen evolution reaction (HER) and oxygen evolution reaction (OER). Traditional catalysts, such as Pt and $RuO_2$, facilitate these reactions but contain expensive precious metals. Therefore, more economical electrocatalysts, containing non-noble metals, are desired. One such class of materials are perovskite oxides,[2, 3] which have shown excellent promise in electrocatalysis because of the tunability of their properties by varying the composition, structural order/disorder, and defects modifications, as well as their stability in different conditions. Several perovskite oxides, such as the benchmark catalyst $Ba_{0.5}Sr_{0.5}Co_{0.8}Fe_{0.2}O_{3-\delta}$ (BSCF),[2] have been utilized to catalyze OER with good efficiency. The perovskite BSCF has attracted much attention due to its high OER performance in alkaline medium,[4, 5] which is comparable to that of $IrO_2$.[2] Nevertheless, the surface of BSCF is easily amorphized during OER cycles.[6] In addition, it does not perform well for HER catalysis.[7] Studies on the application of some other perovskite oxides for HER have been reproted.[8-10] However, perovskite oxides than can catalyze both OER and HER efficiently are rare. We have recently reported a number of such electrocatalysts based on oxide materials.[11-13] The present study focuses on a perovskite oxide, $Ba_{0.5}Sr_{0.5}Co_{0.5}Mo_{0.5}O_3$ ($BaSrCoMoO_6$). We have previously studied the structural and electrical properties of this material.[14] In the present work, we combine computational and experimental methods to demonstrate the bifunctional electrocatalytic properties of $BaSrCoMoO_6$ for both OER and HER. The activity of this catalyst outperforms that of the benchmark oxide catalyst, BSCF.[2]

## 2. METHODS

**Material Synthesis and Characterization.** Both materials were synthesized using the citrate-nitrate sol-gel method. $Ba(NO_3)_2$ (Alfa Aesar, 99.999%), $Sr(NO_3)_2$ (Alfa Aesar, 99%), $Co(NO_3)_2.6H_2O$ (Acros Organics, 99%), $Fe(NO_3)_3.9H_2O$ (Alfa Aesar, 98.0-101.0%), $(NH_4)_6Mo_7O_{24}.4H_2O$ (Alfa Aesar, 99%), and citric acid monohydrate (Alfa Aesar, 99.5+ %) were used as precursors. The citrate complexing sol-gel method was employed, as previously reported.[3] Briefly, metal nitrates with appropriate molar ratios were dissolved in deionized water to obtain a transparent red solution. Then, citric acid was added as complexing agent to the stirring solution of metal ions. The molar ratio for total metal ions to citric acid was 1:1.1. The solution was continuously heated at 95 ºC on a hotplate to obtain a gel. The dark red gel of $BaSrCoMoO_6$ was further heated at 600 ºC for 6 hours to yield a solid precursor under an argon atmosphere. The powder was then fired at 900 ºC and 1000 ºC for 6 hours for each step and was finally repelletized and sintered at 1100 ºC for 24 hours under argon. Likewise, the dark red gel of $Ba_{0.5}Sr_{0.5}Co_{0.8}Fe_{0.2}O_{3-\delta}$ (BSCF) was obtained using the same process and sintering at different temperatures were done in air (6 hours sintering at each temperature, 600 ºC, 900 ºC, 1000 ºC, and 1100 ºC) to obtain pure phase.

The heating and cooling rate of the furnace was 100 ºC. Powder X-ray diffraction data were obtained at room temperature using Cu Kα1 radiation (λ = 1.54056 Å), and were used for Rietveld refinements using GSAS software and the EXPGUI interface.[15, 16] X-ray photoelectron spectroscopy (XPS) was done at room temperature using Al Kα radiation (1486.7 eV). Iodometric titration was employed to determine the oxygen content (δ), as described elsewhere.[17] 100 mL of stock solution was prepared by dissolving 50 mg of the sample in 1 M HCl solution (purged with Ar for 30 minutes) containing about 2 g KI under argon. Titration of 5 mL stock solution was done with 0.025M $Na_2S_2O_3$ solution, where 5-10 drops of starch were added near the endpoint as an indicator. Titration was performed at least three times under an argon atmosphere for repeatability. The δ values for $BaSrCoMoO_{6-\delta}$ and BSCF were determined to be ~0 and ~0.4, respectively.

**Electrode preparation and electrochemical measurement.** The catalyst ink was prepared by mixing 35 mg of the sample, 40 µL Nafion® D-521 solution (Alfa Aesar, 5% w/w in water and 1-propanol), and finally 7 mL of THF (Alfa Aesar, 99%). This mixture was sonicated for 3 minutes and stirred for 30 minutes. In experiments, where carbon black was sued, 7 mg of carbon black powder (Fuel Cell Store) was added before adding THF. The glassy carbon electrode (5 mm diameter, 0.196 $cm^2$ area, HTW Germany) was polished with 5 µm and 0.3 µm aluminum oxide polishing solution (Allied Hightech Products Inc.) on a polishing cloth, sonicated for 3 minutes in ethanol (Decon Labs, Inc.) and finally washed with DI water before use. Then, the catalyst ink (20 µL) was dropcasted on the surface of the glassy carbon (GC) electrode. The catalyst ink-loaded GC electrode was left to dry in the air for at least 24 hours. The use of the GC electrode is common in OER and HER experiments. Some studies have highlighted the advantages of the GC electrode compared to other types of electrodes.[18] Electrochemical tests for HER and OER activity were performed in a standard three-electrode cell using a rotating disk electrode (Pine Research Instruments). A GC electrode loaded with the catalyst was used as the working electrode. A commercial platinum electrode (for OER) or graphite rod (for HER) (Pine Research Instruments) were used as counter electrode, and Ag/AgCl (in 3 M NaCl, ALS Co., Ltd, Japan) as reference electrode. The resistance of the electrolyte solution (R) during the electrocatalytic experiment was subtracted through iR correction, where the resistance values of ~9 – 30 Ω (HER experiments) and ~47 – 55 Ω (OER experiments) were measured by potentiostatic electrochemical impedance spectroscopy (PEIS) in the frequency range of 100 kHz to 1 Hz. Then, the iR corrected potential versus Ag/AgCl electrode ($E_{Ag/AgCl}$) was recorded, which was converted to potential versus RHE according to the Nernst equation:

$$E_{RHE} = E_{Ag/AgCl} + 0.059\,pH + E^{o}_{Ag/AgCl}$$

where $E^{0}_{vs\ Ag/AgCl} = 0.21V$ for 3M NaCl and 0.197V for saturated KCl for OER and HER measurements, respectively. A 0.1 M (pH = 13.0) or 1 M solution (pH = 14.0) of KOH (Alfa Aesar, Flake, 85%) was prepared in nano pure water (18 MΩ), and purged with argon for at least 30 minutes before each OER or HER experiment. The cyclic voltammetry (CV) profiles were recorded at a scan rate of 10 mV $s^{-1}$ from 0

to 0.8 V and -0.5 to -2.0 V vs Ag/AgCl for OER and HER, respectively. The rotating disk electrode was continuously rotated at 1600 rpm to remove $O_2$ /$H_2$ bubbles evolved at the catalyst surface. Chronopotentiometry (CP) was carried out at a constant current density of 10 mA/cm$^2$. CP experiments were performed by fabricating a two-electrode cell using two 1 cm$^2$ nickel foam electrodes.[8] 100 µL of the catalyst ink was dropcasted on each electrode at 20 µL increment to obtain a total mass loading of ~ 1 mg/cm$^2$. The electrodes were then dried in air overnight. The Ni foam electrodes connected with gold wire and lead connections were separated by a glass fiber filter paper to prevent short-circuiting and crossover and clipped together.

**Density functional theory methods.** The *ab initio* calculations were performed within the density functional theory (DFT) at the level of the spin polarized generalized gradient approximation (SGGA) and the Perdew-Burke-Ernzerhof (PBE)[19] level of approximation augmented by including Hubbard-U corrections[20] based on Dudarev's approach,[21] as implemented in the Vienna Ab-initio Simulation Package (VASP).[22-24] The projected augmented wave (PAW) potential [23, 24] was used to describe the core electrons. The Hubbard-U parameter was applied as a many-body correction to overcome the underestimation of electronic correlation due to the approximate nature of the exchange-correlation functionals in the traditional single particle Kohn-Sham DFT. It partially corrects the electronic self-interaction error inherent in DFT and leads to better gap estimations. Hubbard parameters were used only for the d-orbitals of the transition metal (TM) atoms. After testing a range of U values, U(d,TM) =3 eV was selected for Co, Mo and Fe. This value is very close to other DFT/SGGA + U studies reported on similar systems.[25-31] We note that the use of DFT/SGGA+U has been shown to work very well for ternary alloys of the type $ABO_3$ by producing correct total energies and band gap values.[32]
The $ABO_3$ perovskite-type $BaSrCoMoO_6$ and $Ba_{0.5}Sr_{0.5}Co_{0.8}Fe_{0.2}O_{3-\delta}$ ($\delta = 0.4$) systems were simulated by supercells periodically repeated along the x, y and z-directions. The supercells for $BaSrCoMoO_6$ were obtained by extending a $BaSrCoMoO_6$ unit cell with *Fm*-3*m* symmetry. Supercells of several sizes were considered. Positions of Ba and Sr atoms were randomly selected, while ordering was maintained for the Co and Mo atoms, consistent with the experimentally determined structure. Among various supercells considered with 20, 40, or 80 atoms, a 40 atom supercell with $P4_222$ symmetry was found to have the optimal energetics (lowest energy per atom). Similarly, for $Ba_{0.5}Sr_{0.5}Co_{0.8}Fe_{0.2}O_{3-\delta}$, different sizes of supercells with 46 and 92 atoms were considered. They were obtained by extending the $BaCoO_3$ unit cell with *Pm*-3*m* symmetry. In each of the supercells, the placing of Ba and Sr atoms were random. This was also the case for Co and Fe atoms, consistent with the experimentally determined structure. The oxygen vacancy sites were also chosen randomly. A 92 atom supercell with *P*1 symmetry was found to have the optimal energetics. A Monkhorst- Pack 4x4x4 k-point mesh was used in all calculations.[33] All structures were subjected to full symmetry unconstrained geometric relaxation of all atom positions and cell parameters. We note that the relaxation of the cell volume is extremely critical for an accurate estimation of the ground state. The lowest energy structures obtained in the two cases were used in the calculation of band structures and densities of states (DOS).

## 3. Results and Discussion

**3.1. Structural Characterization.** Both $BaSrCoMoO_6$ and BSCF belong to the perovskite family, represented by the general formula $ABO_3$ (A = Ba/Sr, B = Co/Mo or Co/Fe). Both oxides have cubic structures, but with different space groups, *Fm-3m*[23-25] for $BaSrCoMoO_6$ and *Pm-3m*[17] for

BSCF. As we have previously described,[14] the structure of $BaSrCoMoO_6$, consists of six-coordinated $Co^{2+}$ and $Mo^{6+}$ ions, which are ordered in the material lattice (Figure 1a).

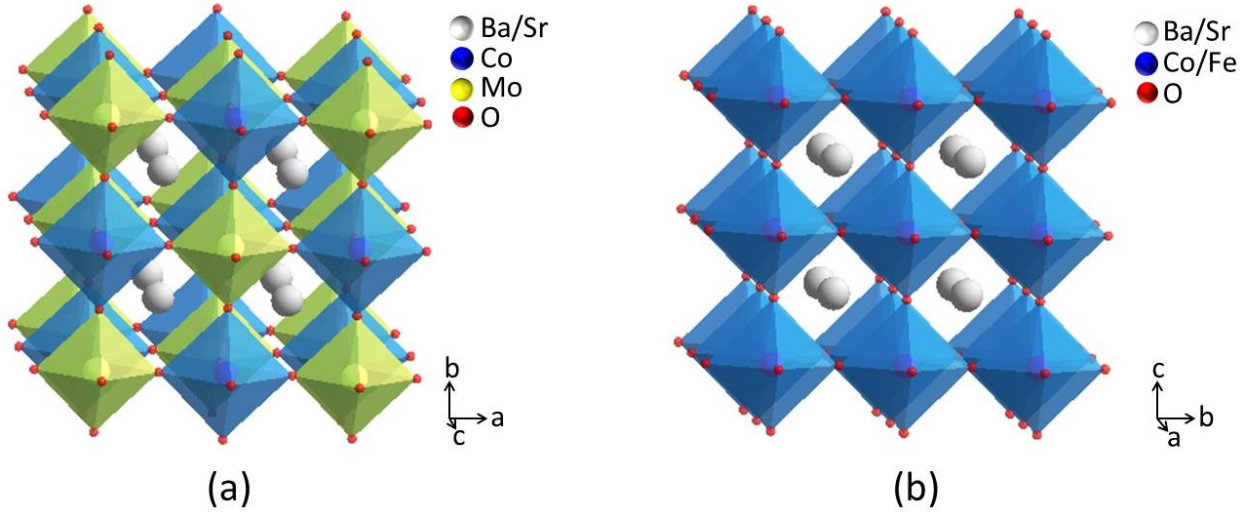


**Figure 1**. (a) Crystal structure of $Ba_{0.5}Sr_{0.5}Co_{0.5}Mo_{0.5}O_3$ ($BaSrCoMoO_6$). Note the ordering of Co and Mo. (b) Crystal structure of $Ba_{0.5}Sr_{0.5}Co_{0.8}Fe_{0.2}O_{3-\delta}$.

**Table 1**: The refined structural parameters of $BaSrCoMoO_6$ using powder X-ray diffraction data. Space group: *Fm-3m* (#225) a = 7.9913(1) Å, $R_p$ = 0.0396, $wR_p$ = 0.0549, $\chi^2$ = 2.92%.

| Element | *x* | *y* | *z* | Occupancy | Uiso | Multiplicity |
|---|---|---|---|---|---|---|
| Ba1/Sr1 | 0.25 | 0.25 | 0.25 | 0.5 | 0.017(6) | 8 |
| Co1 | 0.5 | 0.5 | 0.5 | 1 | 0.013(2) | 4 |
| Mo1 | 0 | 0 | 0 | 1 | 0.014(1) | 4 |
| O1 | 0.2428(7) | 0 | 0 | 1 | 0.014(2) | 24 |

**Table 2**: The refined structural parameters of $Ba_{0.5}Sr_{0.5}Co_{0.8}Fe_{0.2}O_{3-\delta}$ (BSCF) using powder X-ray diffraction data. Space group: *Pm-3m* (#221) a = 3.99413(24) Å, $R_p$ = 0.0175, $wR_p$ = 0.0260, $\chi^2$ = 1.45%.

| Element | *x* | *y* | *z* | Occupancy | Uiso | Multiplicity |
|---|---|---|---|---|---|---|
| Ba1/Sr1 | 0.5 | 0.5 | 0.5 | 0.5/0.5 | 0.0210(5) | 1 |
| Co1/Fe1 | 0 | 0 | 0 | 0.8/0.2 | 0.0300(7) | 1 |
| O1 | 0.5 | 0 | 0 | 1 | 0.071(2) | 3 |

On the other hand, BSCF does not have such ordering pattern and both Fe and Co share the same crystallographic site (Figure 1b).[17] Figures 2 shows the Rietveld refinement profiles, and Tables 1 and 2 list the refined structural parameters of these materials. Scanning electron microscopy (SEM) data show larger grain size for $BaSrCoMoO_6$ compared to BSCF, as demonstrated in Figures 3.

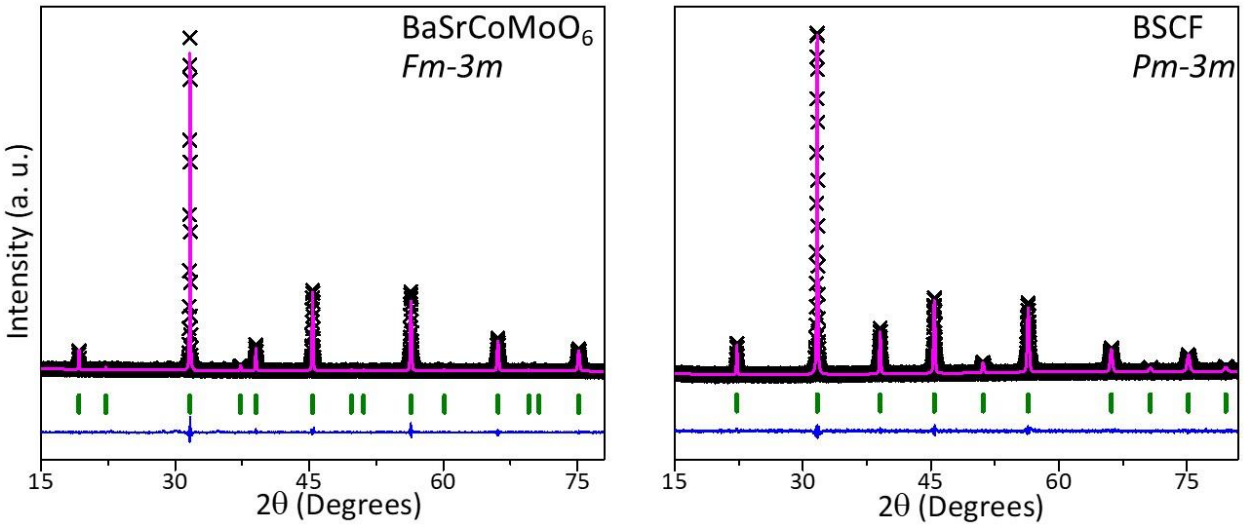


**Figure 2**. Rietveld refinement profiles using powder X-ray diffraction data. Black crosses, magenta solid curve, olive vertical tick marks, and the lower blue curve correspond to the experimental data, the calculated pattern for the cubic models, the Bragg peak positions, and the difference plot, respectively.

In addition, the transmission electron microscopy (TEM) mapping for both compounds show a uniform distribution of metals, as demonstrated in Figures 4 and 5. The X-ray photoelectron spectroscopy (XPS) data for $BaSrCoMoO_6$ indicate $Co^{2+}$ and $Mo^{6+}$ (Figure 6), consistent with our previous study.[14] For BSCF, the oxidation states of transition metals have been previously reported based on XPS and EELS. [34, 35] Our XPS data (Figure 7) are similar to those reported previously.[34] In that work, the oxidation state of cobalt was assigned to be primarily +3, based on the binding energy of the cobalt peak, which is similar to our observation. However, another study based on electron energy-loss spectroscopy (EELS) concluded that in addition to trivalent, there is also some divalent cobalt in BSCF.[35] Regarding the iron oxidation state, the low concentration of iron in this compound leads to a broad XPS spectrum both in our data and in the data reported by others,[34] where the presence of mostly $Fe^{3+}$ and some $Fe^{4+}$ was suggested.[34]

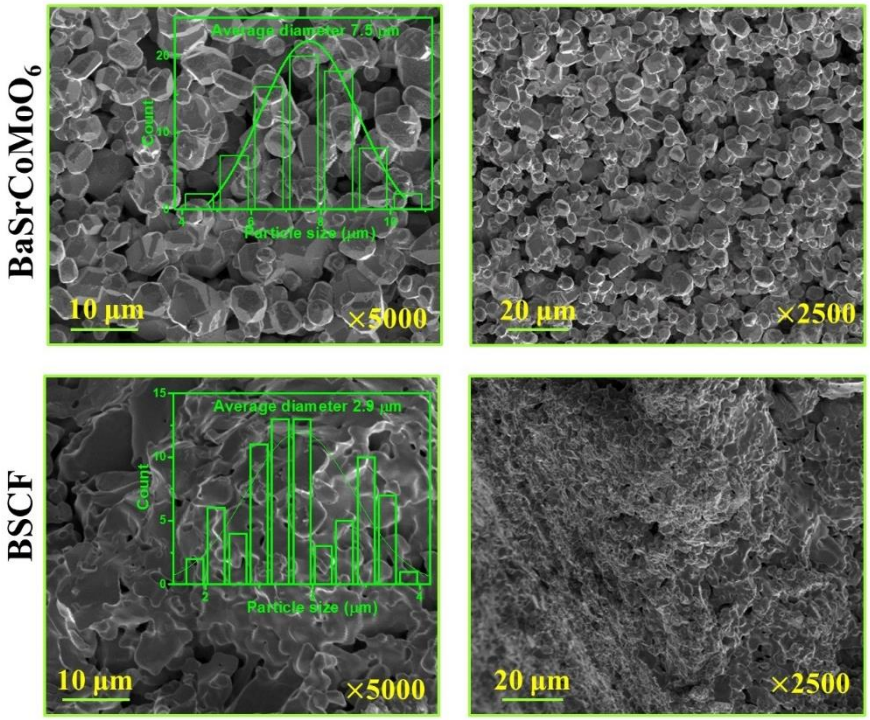


**Figure 3.** Scanning electron microscopy images of both materials. The insets on the left panel show the histograms and Gaussian fit analysis for the average diameter of crystallites.

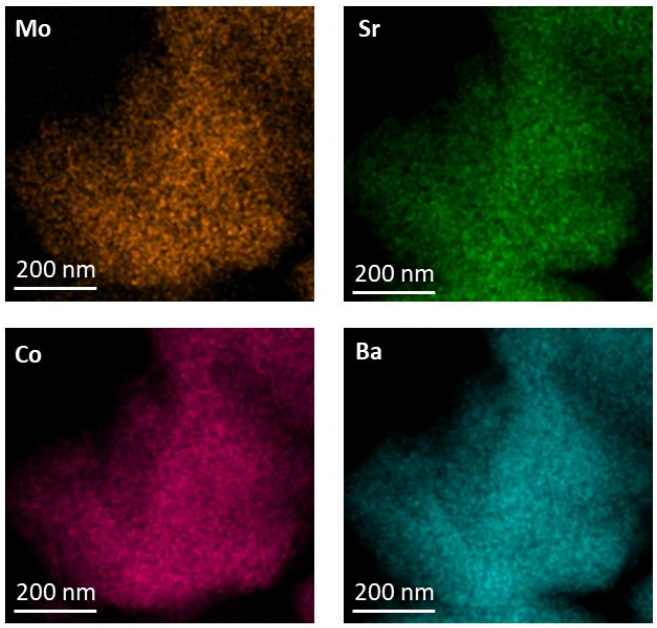


**Figure 4.** Transmission electron microscopy elemental map for $BaSrCoMoO_6$.

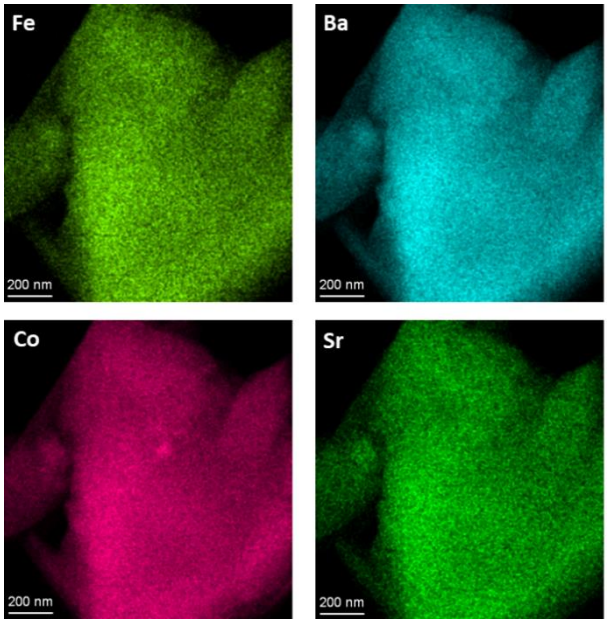


**Figure 5.** Transmission electron microscopy elemental map for BSCF.

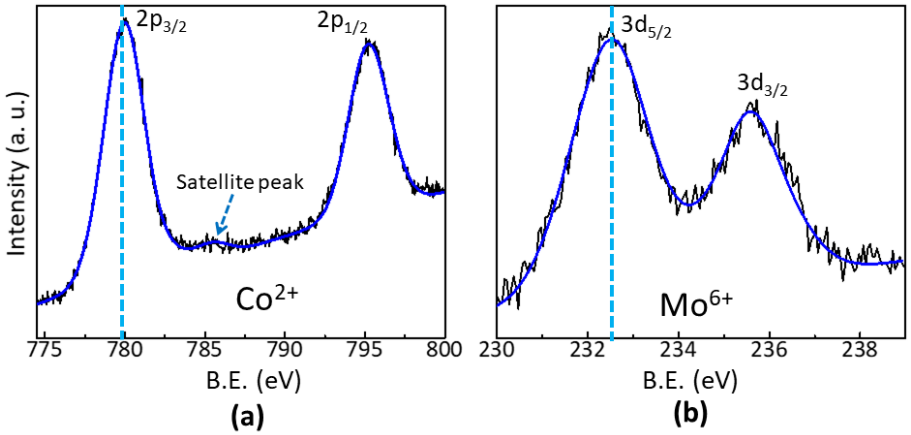


**Figure 6.** X-ray photoelectron spectroscopy spectra for $BaSrCoMoO_6$: (a) cobalt and (b) molybdenum.

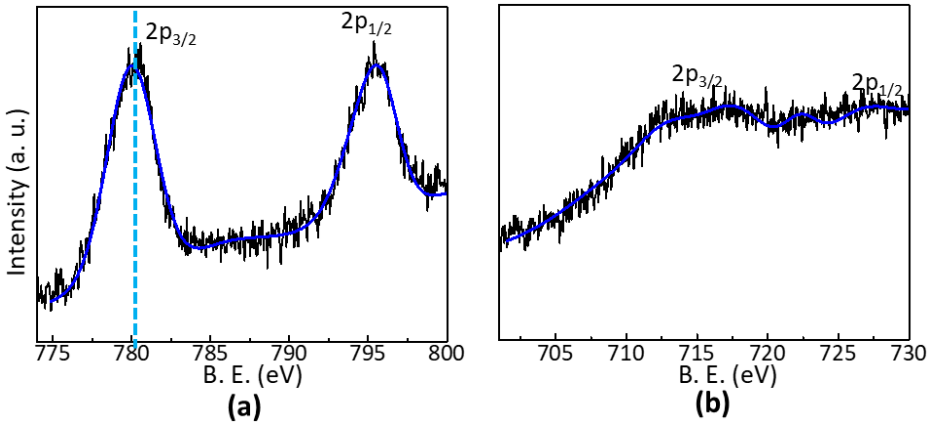


**Figure 7.** X-ray photoelectron spectroscopy data for BSCF, showing the spectra for (a) cobalt and (b) iron.

### 3.2. Enhancement of Electrocatalytic Properties for HER

The variations in composition and structure have a significant impact on HER and OER activities. As shown in Figures 8a, HER experiments in 1 M KOH show the enhanced electrocatalytic performance of $BaSrCoMoO_6$ over BSCF.

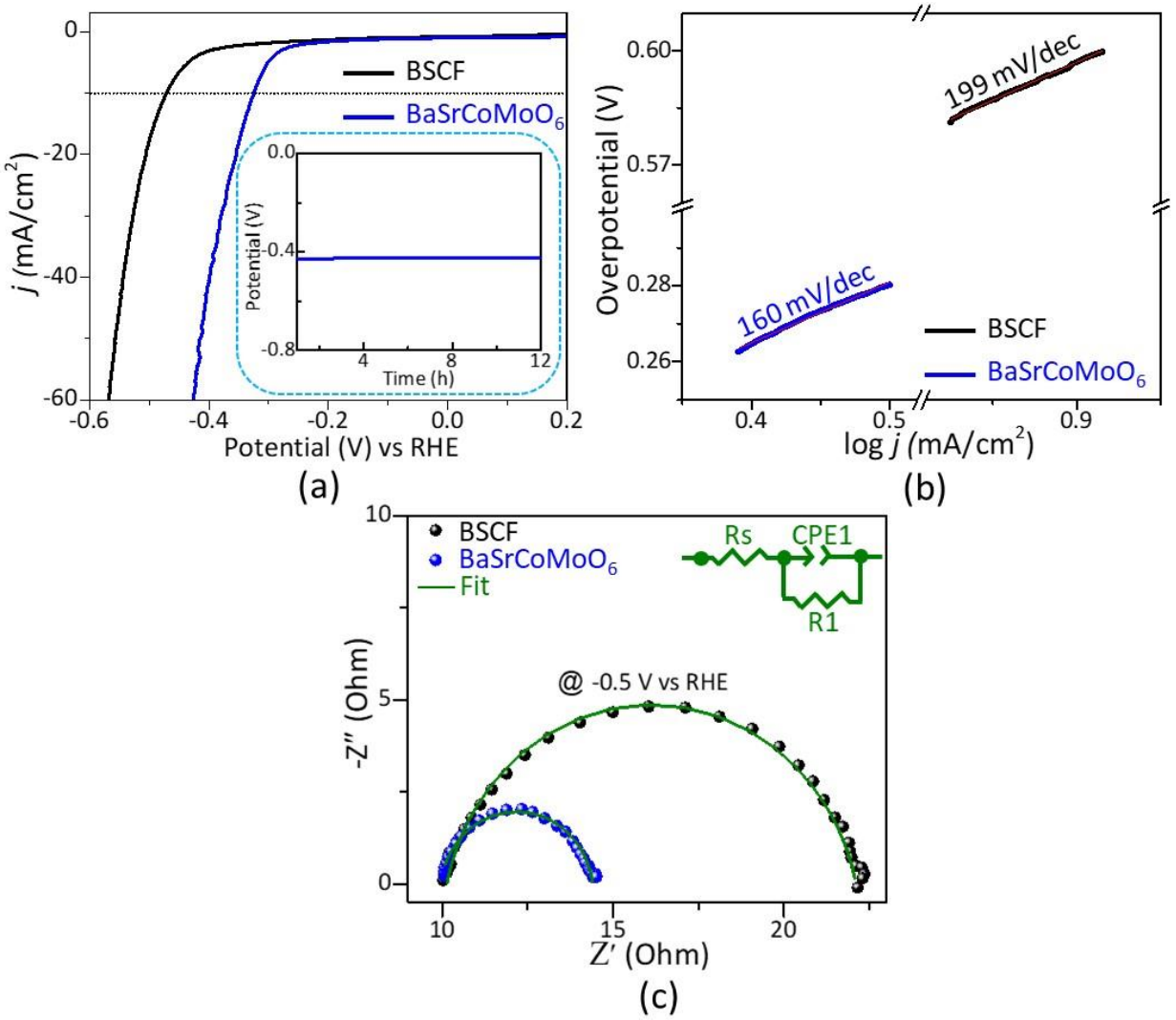


**Figure 8.** (a) HER polarization curves in 1 M KOH. The inset shows the chronopotentiometry data of $BaSrCoMoO_6$ at a current density of 10 mA/cm$^2$. (b) The Tafel plot showing Tafel slopes. (c) The Nyquist plot recorded in the HER potential region, −0.5 V vs the RHE, indicating lower charge transfer resistance for $BaSrCoMoO_6$. Inset shows the equivalent circuit model that represents the fit (green curve) to the EIS data.

The overpotential ($\eta_{10}$) values required to deliver a current density of 10 mA/cm$^2$ are 325 mV and 470 mV, respectively. The current density of 10mA/cm$^2$ is typically adopted as a reference in such studies, as desired for 10% solar-to-fuel conversion efficiency.[7] The observed overpotential for BSCF is close to that of a previous report, $\eta_{10}$ = 430 mV.[7] The overpotential of $BaSrCoMoO_6$ is significantly lower than that of BSCF. It is also lower than the values reported for some other highly active perovskite-based electrocatalysts such as $Ba_{0.95}Co_{0.4}Fe_{0.4}Zr_{0.1}Y_{0.1}O_{3-\delta}$ ($\eta_{10}$ = 360 mV)[7] and $SrCo_{0.7}Fe_{0.25}Mo_{0.05}O_{3-\delta}$ ($\eta_{10}$ = 378 mV).[36] In addition, $BaSrCoMoO_6$ is very stable, as evident from the nearly constant chronopotentiometry response, shown in the inset of Figure 8a.

To examine the kinetics of the reaction, the Tafel equation, $\eta = a + b \log j$, was used where $\eta$ is the overpotential, and $j$ is the current density. The Tafel slope, *i.e.,* the slope of $\eta$ versus log $j$, indicates the kinetics of the reaction.[37, 38] Tafel plot is influenced by the conductivity and mass transport of the catalyst.[39-41] In general, a smaller Tafel slope indicates a faster reaction. As shown in Figure 8b, $BaSrCoMoO_6$ shows a smaller value of Tafel slope, 142 mV/dec, compared to BSCF, 174 mV/dec, indicating the faster electron transfer in $BaSrCoMoO_6$ during the HER. This catalyst also shows smaller charge transfer resistance[8] in the HER region (-0.5 V vs RHE), as evident from the lower real axis intercept of the semi-circle in Nyquist plot as compared to BSCF (Figure 8c).

### 3.3. Enhancement of Electrocatalytic Properties for OER

$BaSrCoMoO_6$ also shows an enhanced performance for OER electrocatalysis compared with BSCF.[4, 42, 43] As shown in Figure 9a, the overpotential ($\eta_{10}$) at 10 mA/cm$^2$ is 400 mV for $BaSrCoMoO_6$, as compared to that of BSCF, 500 mV, in 0.1 M KOH. The overpotential for BSCF is in line with previous reports.[4, 42, 43] We note that the OER activity of $BaSrCoMoO_6$ is comparable to that of the precious metal catalyst, $RuO_2$ ($\eta_{10}$ = 420 mV).[13, 44]

The kinetics of the OER for $BaSrCoMoO_6$ is faster than that of BSCF, as evident from the Tafel plots[37, 38, 45] shown in Figure 9b, giving Tafel slopes of 93 mV/dec for $BaSrCoMoO_6$, as compared to 81 mV/dec for BSCF. The lower Tafel slope value for the former is indicative of faster reaction, consistent with its greater OER activity. In addition, the charge transfer resistance in the OER region (1.7 V vs RHE) is smaller for $BaSrCoMoO_6$ than BSCF (Figure 9c), which indicates an enhanced charge transfer for $BaSrCoMoO_6$, consistent with its superior catalytic activity. This catalyst is also very stable, as evident from the stable chronopotentiometry response in OER conditions, shown in the inset of Figure 9a.

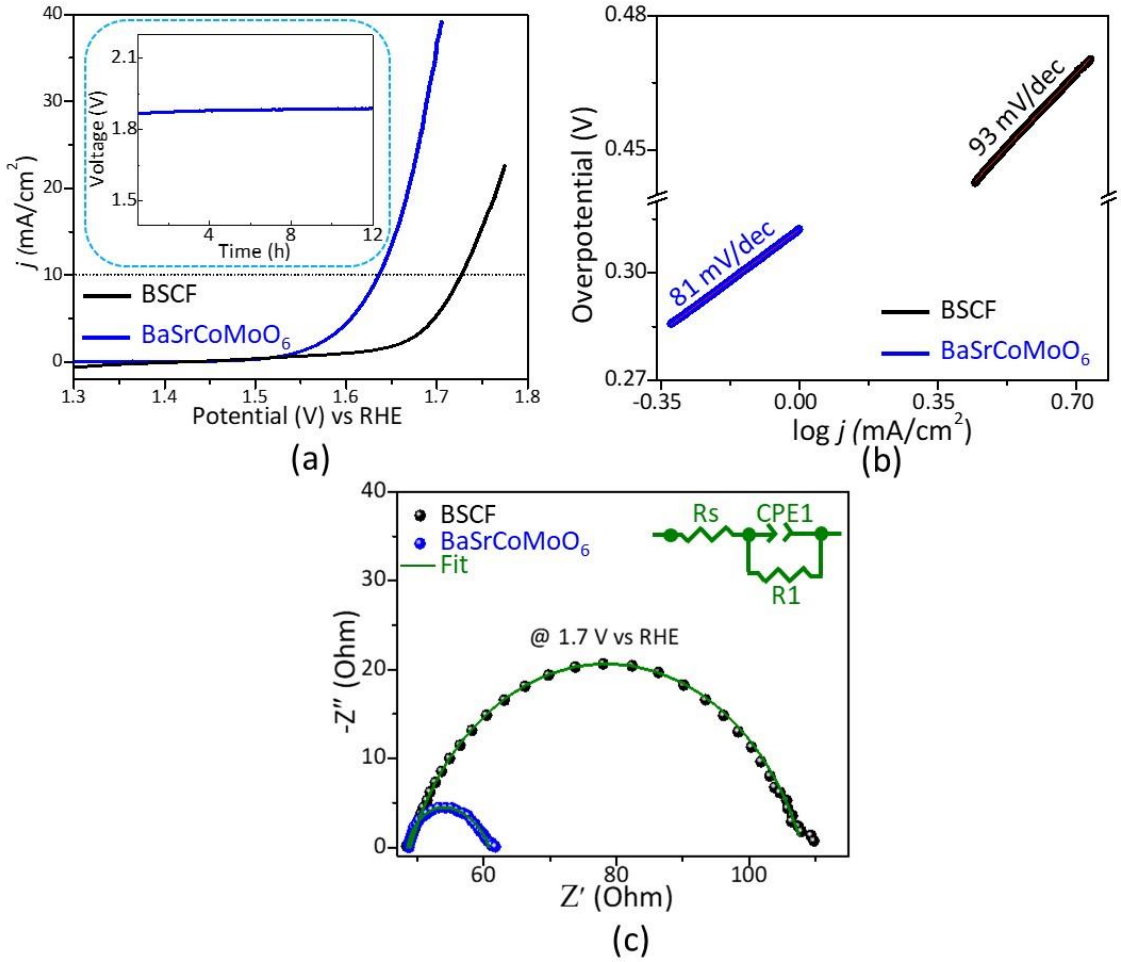


**Figure 9.** (a) OER polarization curves in 0.1 M KOH. The inset shows the chronopotentiometry data for $BaSrCoMoO_6$ at a current density of 10 mA/cm$^2$. (b) The Tafel plot showing Tafel slopes. (c) The Nyquist plot recorded in the OER potential region, 1.7 V vs the RHE, indicating lower charge transfer resistance for $BaSrCoMoO_6$. Inset shows the equivalent circuit model that represents the fit (green curve) to the EIS data.

Another important advantage of $BaSrCoMoO_6$ is that it can be used in bulk without the need for nanofabrication or composite formation. Even the addition of carbon black, which is routinely added in OER or HER studies, is not needed. Carbon black is often mixed with the catalyst to enhance the change transfer.[46-48] The electrocatalytic experiments for $BaSrCoMoO_6$ with or without carbon black lead to similar overpotentials (Figure 10). This indicates the outstanding intrinsic catalytic activity of $BaSrCoMoO_6$. On the other hand, for BSCF, the absence of carbon black leads to low catalytic performance, where the current response does not even reach 10 $mA/cm^2$, as shown in Figure 10.

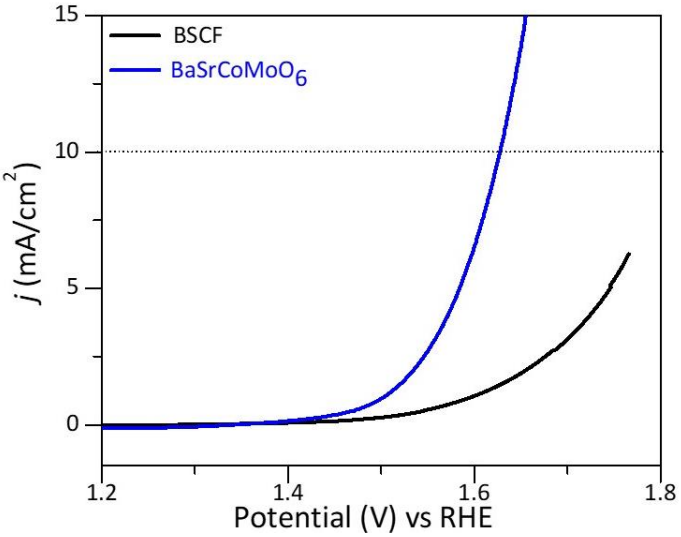


**Figure 10.** Representative polarization curve showing the OER activity without the addition of carbon black for $BaSrCoMoO_6$ and BSCF.

Importantly, $BaSrCoMoO_6$ retains its structural integrity, as evident from X-ray diffraction data before and after 1000 cycles of OER and HER. As shown in Figure 11, the X-ray diffraction pattern remains unchanged, indicating the catalyst structure is intact.

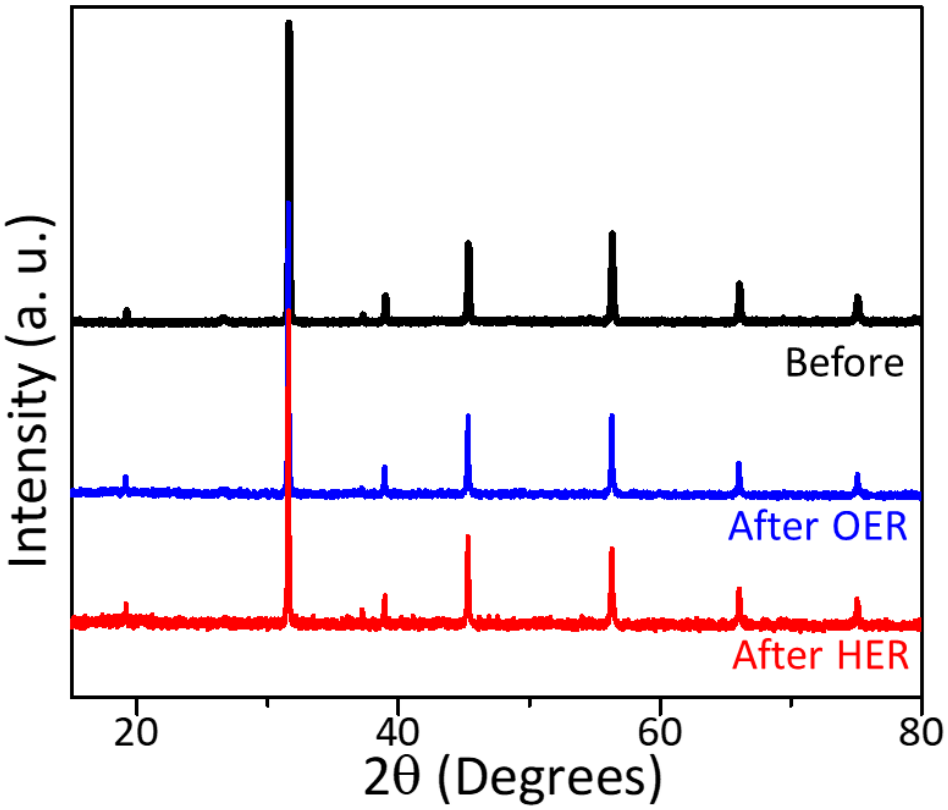


**Figure 11.** X-ray diffraction data before and after 1000 cycles of OER and HER.

### 3.4. Density Functional Theory (DFT) Calculations

Further insight into the properties of these materials is obtained using density functional theory (DFT) calculations. These calculations (Figure 12) indicate that, for $BaSrCoMoO_6$, the center of the Co *d*-band is considerably closer to the Femi level, compared to that of BSCF. This is important because cobalt in BSCF is considered the active site,[2] and its electronic configuration is thought to be responsible for the high electrocatalytic activity of BSCF.[2] Therefore, the shift in the Co *d*-band center can have a direct impact on the electrocatalytic performance.

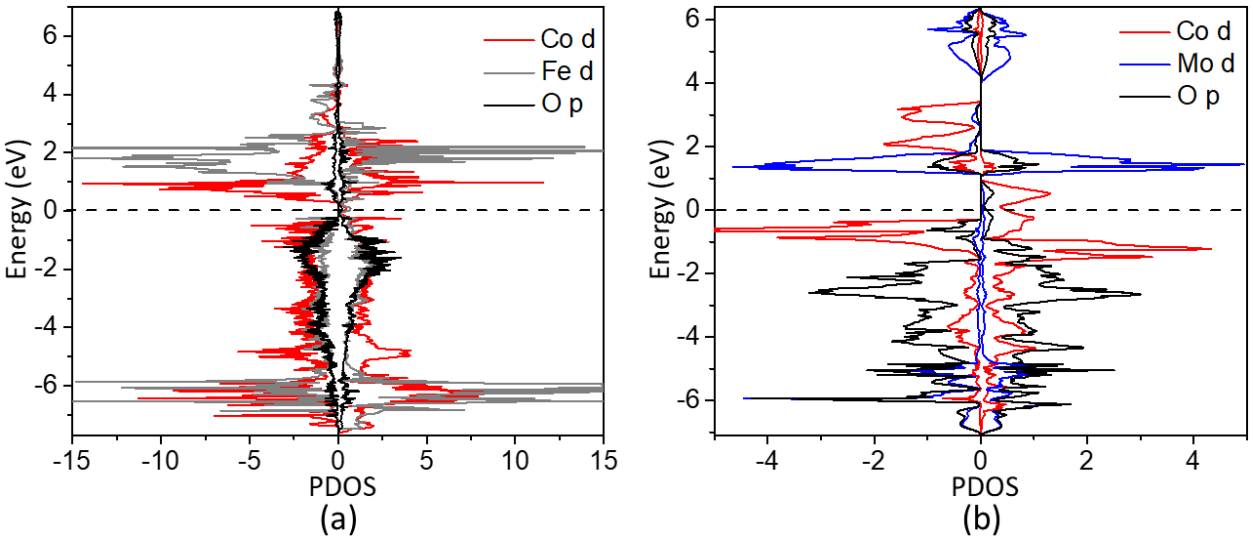


**Figure 12.** Density of States (DOS) from DFT calculations for (a) BSCF, and (b) $BaSrCoMoO_6$.

It has been previously proposed[49, 50] that the proximity of the *d*-band center to the Fermi level is correlated with the electrocatalytic activity due to the improved bonding with the adsorbates during the reaction.[49, 50] The average center of the Co *d*-band (from both spin up and spin down) for BSCF is -3.796 eV, as compared to that of $BaSrCoMoO_6$, -1.852 eV, indicating a significant shift toward the Fermi level. The average center of the Mo *d*-band in $BaSrCoMoO_6$ is -5.204 eV, while that of the Fe *d*-band for BSCF is -4.193 eV. The difference in the *d*-band centers of Mo and Fe is expected. However, the magnitude of this difference is about half the difference between the centers of Co *d*-bands of the two materials. The enhanced electrocatalytic performance of $BaSrCoMoO_6$ is consistent with the considerable shift of the Co *d*-band closer to the Fermi level compared to that of BSCF.

**Conclusions.** In summary, we have demonstrated the importance of compositional modification and structural order in the design of highly active oxide electrocatalysts. The new catalyst, $BaSrCoMoO_6$ shows significantly greater electrocatalytic activity compared to the well-known catalyst $Ba_{0.5}Sr_{0.5}Co_{0.8}Fe_{0.2}O_{3-\delta}$ (BSCF). Both OER and HER processes are catalyzed more effectively using $BaSrCoMoO_6$, which also has an additional advantage, namely its ability to act as an efficient electrocatalyst without the need for nanofabrication, composite formation, or any additives.

**Acknowledgement.** This work is supported by the National Science Foundation (NSF) under grant no. DMR-1943085.

**References**

1. Wang, C.; Shang, H.; Xu, H.; Du, Y., Nanoboxes endow non-noble-metal-based electrocatalysts with high efficiency for overall water splitting. *J. Mater. Chem. A* **2021,** *9*, 857-874.
2. Suntivich, J.; May, K. J.; Gasteiger, H. A.; Goodenough, J. B.; Shao-Horn, Y., A Perovskite Oxide Optimized for Oxygen Evolution Catalysis from Molecular Orbital Principles. *Science* **2011,** *334*, 1383.
3. Hona, R. K.; Ramezanipour, F., Remarkable Oxygen-Evolution Activity of a Perovskite Oxide from the $Ca_{2-x}Sr_xFe_2O_{6-\delta}$ Series. *Angew. Chem.* **2019,** *58*, 2060-2063.
4. Xu, X.; Pan, Y.; Zhou, W.; Chen, Y.; Zhang, Z.; Shao, Z., Toward Enhanced Oxygen Evolution on Perovskite Oxides Synthesized from Different Approaches: A Case Study of $Ba_{0.5}Sr_{0.5}Co_{0.8}Fe_{0.2}O_{3-\delta}$. *Electrochim. Acta* **2016,** *219*, 553-559.
5. Sun, H.; Chen, G.; Zhu, Y.; Liu, B.; Zhou, W.; Shao, Z., B-Site Cation Ordered Double Perovskites as Efficient and Stable Electrocatalysts for Oxygen Evolution Reaction. *Chem. Eur. J.* **2017,** *23*, 5722-5728.
6. May, K. J.; Carlton, C. E.; Stoerzinger, K. A.; Risch, M.; Suntivich, J.; Lee, Y.-L.; Grimaud, A.; Shao-Horn, Y., Influence of Oxygen Evolution during Water Oxidation on the Surface of Perovskite Oxide Catalysts. *J. Phys. Chem. Lett.* **2012,** *3*, 3264-3270.
7. Li, X.; He, L.; Zhong, X.; Zhang, J.; Luo, S.; Yi, W.; Zhang, L.; Hu, M.; Tang, J.; Zhou, X.; Zhao, X.; Xu, B., Evaluation of A-Site $Ba^{2+}$-Deficient $Ba_{1-x}Co_{0.4}Fe_{0.4}Zr_{0.1}Y_{0.1}O_{3-\delta}$ Oxides as Electrocatalysts for Efficient Hydrogen Evolution Reaction. *Scanning* **2018,** *2018*, 1341608-1341608.
8. Wang, J.; Gao, Y.; Chen, D.; Liu, J.; Zhang, Z.; Shao, Z.; Ciucci, F., Water Splitting with an Enhanced Bifunctional Double Perovskite. *ACS Catal.* **2018,** *8*, 364-371.
9. Karki, S. B.; Ramezanipour, F., Pseudocapacitive Energy Storage and Electrocatalytic Hydrogen-Evolution Activity of Defect-Ordered Perovskites $Sr_xCa_{3-x}GaMn_2O_8$ (x = 0 and 1). *ACS Appl. Energy Mater.* **2020,** *3*, 10983−10992.

10. Alom, M. S.; Kananke-Gamage, C. C. W.; Ramezanipour, F., Perovskite Oxides as Electrocatalysts for Hydrogen Evolution Reaction. *ACS Omega* **2022,** *7*, 7444-7451.
11. Hona, R. K.; Karki, S. B.; Cao, T.; Mishra, R.; Sterbinsky, G. E.; Ramezanipour, F., Sustainable Oxide Electrocatalyst for Hydrogen and Oxygen-Evolution Reactions. *ACS Catal.* **2021,** *11*, 14605−14614.
12. Karki, S. B.; Andriotis, A. N.; Menon, M.; Ramezanipour, F., Bifunctional Water-Splitting Electrocatalysis Achieved by Defect-Order in $LaA_2Fe_3O_8$ (A = Ca, Sr). *ACS Appl. Energy Mater.* **2021,** *4*, 12063−12066.
13. Hona, R. K.; Karki, S. B.; Ramezanipour, F., Oxide Electrocatalysts Based on Earth-Abundant Metals for Both Hydrogen- and Oxygen-Evolution Reactions. *ACS Susttain. Chem. Eng.* **2020,** *8*, 11549-11557.
14. Karki, S. B.; Ramezanipour, F., Magnetic and electrical properties of $BaSrMMoO_6$ (M = Mn, Fe, Co, and Ni). *Mater. Today Chem.* **2019,** *13*, 25-33.
15. Larson, A. C.; Von Dreele, A. C., *General Structure Analysis System (GSAS), Los Alamos National Laboratory Report LAUR* **2004**, 86 - 748.
16. Toby, B. H., EXPGUI, a graphical user interface for GSAS. *J. Appl. Crystallogr.* **2001,** *34*, 210−213.
17. Hona, R. K.; Huq, A.; Mulmi, S.; Ramezanipour, F., Transformation of Structure, Electrical Conductivity, and Magnetism in $AA'Fe_2O_{6-\delta}$, A = Sr, Ca and A′ = Sr. *Inorg. Chem.* **2017,** *56*, 9716-9724.
18. Fiegenbaum, F.; de Souza, M. O.; Becker, M. R.; Martini, E. M. A.; de Souza, R. F., Electrocatalytic activities of cathode electrodes for water electrolysis using tetra-alkyl-ammonium-sulfonic acid ionic liquid as electrolyte. *J. Power Sources* **2015,** *280*, 12-17.
19. Perdew, J. P.; Burke, K.; Ernzerhof, M., Generalized Gradient Approximation Made Simple. *Phys. Rev. Lett.* **1996,** *77*, 3865-3868.
20. Andriotis, A. N.; Mpourmpakis, G.; Lisenkov, S.; Sheetz, R. M.; Menon, M., U-calculation of the LSDA + U functional using the hybrid B3LYP and HSE functionals. *Phys. Status Solidi B* **2013,** *250*, 356-363.
21. Dudarev, S. L.; Botton, G. A.; Savrasov, S. Y.; Humphreys, C. J.; Sutton, A. P., Electron-energy-loss spectra and the structural stability of nickel oxide: An LSDA+U study. *Phys. Rev. B* **1998,** *57*, 1505-1509.
22. Kresse, G.; Hafner, J., Ab initio molecular dynamics for liquid metals. *Phys. Rev. B* **1993,** *47*, 558-561.
23. Kresse, G.; Joubert, D., From ultrasoft pseudopotentials to the projector augmented-wave method. *Phys. Rev. B* **1999,** *59*, 1758-1775.
24. Blöchl, P. E., Projector augmented-wave method. *Phys. Rev. B* **1994,** *50*, 17953-17979.
25. Ding, H.; Virkar, A. V.; Liu, M.; Liu, F., Suppression of Sr surface segregation in $La_{1-x}Sr_xCo_{1-y}Fe_yO_{3-\delta}$: a first principles study. *Phys. Chem. Chem. Phys.* **2013,** *15*, 489-496.
26. Cai, Z.; Kuru, Y.; Han, J. W.; Chen, Y.; Yildiz, B., Surface Electronic Structure Transitions at High Temperature on Perovskite Oxides: The Case of Strained $La_{0.8}Sr_{0.2}CoO_3$ Thin Films. *J. Am. Chem. Soc.* **2011,** *133*, 17696-17704.
27. Rollmann, G.; Rohrbach, A.; Entel, P.; Hafner, J., First-principles calculation of the structure and magnetic phases of hematite. *Phys. Rev. B* **2004,** *69* (16), 165107.
28. Wang, L.; Maxisch, T.; Ceder, G., Oxidation energies of transition metal oxides within the GGA+U framework. *Phys. Review B* **2006,** *73*, 195107.
29. Han, J. W.; Yildiz, B., Enhanced one dimensional mobility of oxygen on strained $LaCoO_3$(001) surface. *J. Mater. Chem.* **2011,** *21*, 18983-18990.
30. Andriotis, A. N.; Sheetz, R. M.; Menon, M., LSDA+U method: A calculation of the U values at the Hartree-Fock level of approximation. *Phys. Rev. B* **2010,** *81*, 245103.
31. Andriotis, A. N.; Fthenakis, Z. G.; Menon, M., Successive spin polarizations underlying a new magnetic coupling contribution in diluted magnetic semiconductors. *J. Phys.: Condens. Matter.* **2015,** *27*, 052202.

32. Varignon, J.; Bibes, M.; Zunger, A., Origin of band gaps in 3d perovskite oxides. *Nat. Commun.* **2019,** *10*, 1658.
33. Monkhorst, H. J.; Pack, J. D., Special points for Brillouin-zone integrations. *Phys. Rev. B* **1976,** *13*, 5188-5192.
34. Jung, J.-I.; Edwards, D. D., X-ray photoelectron (XPS) and Diffuse Reflectance Infra Fourier Transformation (DRIFT) study of $Ba_{0.5}Sr_{0.5}Co_xFe_{1-x}O_{3-\delta}$ (BSCF: x=0–0.8) ceramics. *J. Solid State Chem.* **2011,** *184* (8), 2238-2243.
35. Arnold, M.; Xu, Q.; Tichelaar, F. D.; Feldhoff, A., Local Charge Disproportion in a High-Performance Perovskite. *Chem. Mater.* **2009,** *21*, 635-640.
36. Zhang, Z.; Chen, Y.; Dai, Z.; Tan, S.; Chen, D., Promoting hydrogen-evolution activity and stability of perovskite oxides via effectively lattice doping of molybdenum. *Electrochim. Acta* **2019,** *312*, 128-136.
37. Bard, A. J.; Faulkner, L. R., *Electrochemical Methods: Fundamentals and Applications*. Wiley: 2000, New York.
38. Oh, S.; Kim, H.; Kwon, Y.; Kim, M.; Cho, E.; Kwon, H., Porous Co–P foam as an efficient bifunctional electrocatalyst for hydrogen and oxygen evolution reactions. *J. Mater. Chem. A* **2016,** *4*, 18272-18277.
39. Song, F.; Bai, L.; Moysiadou, A.; Lee, S.; Hu, C.; Liardet, L.; Hu, X., Transition Metal Oxides as Electrocatalysts for the Oxygen Evolution Reaction in Alkaline Solutions: An Application-Inspired Renaissance. *J. Am. Chem. Soc.* **2018,** *140*, 7748-7759.
40. Moir, J.; Soheilnia, N.; O'Brien, P.; Jelle, A.; Grozea, C. M.; Faulkner, D.; Helander, M. G.; Ozin, G. A., Enhanced Hematite Water Electrolysis Using a 3D Antimony-Doped Tin Oxide Electrode. *ACS Nano* **2013,** *7*, 4261-4274.
41. Song, F.; Hu, X., Ultrathin Cobalt–Manganese Layered Double Hydroxide Is an Efficient Oxygen Evolution Catalyst. *J. Am. Chem. Soc.* **2014,** *136*, 16481-16484.
42. Zhu, Y.; Zhou, W.; Chen, Z.-G.; Chen, Y.; Su, C.; Tadé, M. O.; Shao, Z., $SrNb_{0.1}Co_{0.7}Fe_{0.2}O_{3-\delta}$ Perovskite as a Next-Generation Electrocatalyst for Oxygen Evolution in Alkaline Solution. *Angew. Chem* **2015,** *54*, 3897-3901.
43. Zhu, Y.; Zhou, W.; Sunarso, J.; Zhong, Y.; Shao, Z., Phosphorus-Doped Perovskite Oxide as Highly Efficient Water Oxidation Electrocatalyst in Alkaline Solution. *Adv. Funct. Mater* **2016,** *26*, 5862-5872.
44. Das, D.; Das, A.; Reghunath, M.; Nanda, K. K., Phosphine-free avenue to $Co_2P$ nanoparticle encapsulated N,P co-doped CNTs: a novel non-enzymatic glucose sensor and an efficient electrocatalyst for oxygen evolution reaction. *Green Chem.* **2017,** *19*, 1327-1335.
45. Pan, Y.; Chen, Y.; Li, X.; Liu, Y.; Liu, C., Nanostructured nickel sulfides: phase evolution, characterization and electrocatalytic properties for the hydrogen evolution reaction. *RSC Adv.* **2015,** *5*, 104740-104749.
46. Jin, C.; Cao, X.; Zhang, L.; Zhang, C.; Yang, R., Preparation and electrochemical properties of urchin-like $La_{0.8}Sr_{0.2}MnO_3$ perovskite oxide as a bifunctional catalyst for oxygen reduction and oxygen evolution reaction. *J. Power Sources* **2013,** *241*, 225-230.
47. Müller, S.; Striebel, K.; Haas, O., $La_{0.6}Ca_{0.4}CoO_3$: a stable and powerful catalyst for bifunctional air electrodes. *Electrochim. Acta* **1994,** *39*, 1661-1668.
48. Weidenkaff, A.; Ebbinghaus, S. G.; Lippert, T., $Ln_{1-x}A_xCoO_3$ (Ln = Er, La; A = Ca, Sr)/Carbon Nanotube Composite Materials Applied for Rechargeable Zn/Air Batteries. *Chem. Mater.* **2002,** *14*, 1797-1805.
49. Sun, Y.; Zhao, Z.; Wu, S.; Li, W.; Wu, B.; Liu, G.; Chen, G.; Xu, B.; Kang, B.; Li, Y.; Li, C., Engineering of the d-Band Center of Perovskite Cobaltite for Enhanced Electrocatalytic Oxygen Evolution. *ChemSusChem* **2020,** *13*, 2671-2676.
50. Sun, S.; Zhou, X.; Cong, B.; Hong, W.; Chen, G., Tailoring the d-Band Centers Endows $(Ni_xFe_{1-x})_2P$ Nanosheets with Efficient Oxygen Evolution Catalysis. *ACS Catal.* **2020,** *10*, 9086-9097.

**TOC Graphic**